A Fast Interferometric Beam Shaper for Multi-Emitter 3D MINFLUX

Maximilian K. Geismann[1,2]*, Alba Gomez-Segalas[1,2]*, Alessandro Passera[1,2], Mehrta Shirzadian[1,2], Francisco Balzarotti[1,#]

[1]Research Institute of Molecular Pathology (IMP), Vienna BioCenter (VBC), Campus-Vienna-Biocenter 1, 1030 Vienna, Austria.

[2]Vienna BioCenter PhD Program, Doctoral School of the University of Vienna and Medical University of Vienna, A-1030, Vienna, Austria

*Equal contribution

[#]Corresponding author: francisco.balzarotti@imp.ac.at

Abstract

Displacing beams of light in a controlled manner is integral to a wide range of optical methods such as scanning microscopes and optical tweezers. Optical super-resolution techniques like STED and RESOLFT, as well as localization techniques like MINFLUX and MINSTED rely on accurate and fast beam displacements. Extending these methods to the third dimension requires axial deflection, which, in contrast to lateral deflection, remains technologically challenging on the microsecond scale. Here, we present a general-purpose beam-shaping polarization interferometer that enables such axial deflections and, based on it, showcase a four-channel dual-color excitation system for three-dimensional MINFLUX imaging and tracking. We include first demonstrations of improved MINFLUX localization schemes that utilize the combination of distinct beam shapes and three-dimensional multi-emitter tracking. We believe that the presented approach will facilitate the broader adoption of three dimensional MINFLUX and provides a versatile basis for future implementations of advanced single-molecule localization methods.

Introduction (without heading)

Displacing and deforming beams of light in a controlled manner is integral to a wide range of optical methods such as scanning microscopes and optical tweezers. Optical super-resolution fluorescence imaging techniques, such as STimulated Emission Depletion (STED)[1], and REversible Saturable Optical Linear Fluorescence Transitions (RESOLFT)[2,3], as well as localization strategies like Maximally INFormative LUminescence eXcitation (MINFLUX)[4] and MINSTED[5], require displacing beams that feature zeros of intensity. In super-resolution imaging techniques, zeros create constrained areas or volumes where a detectable photophysical property of the fluorescent emitters remains unaltered, thus enabling the precise assignment of signal or amplitude on a pixel-by-pixel basis.

MINFLUX[4] stands out as a single-molecule localization strategy, distinguished by its approach of sequentially probing the position of an emitter with different beam shapes. Its high localization efficiency—the number of emitted photons required to reach a given localization precision—has been harvested for stochastic super resolution imaging[6,7] and single-molecule tracking, reaching spatial and temporal resolutions in the nanometer[8] and sub-millisecond[9–11] scales. Beam shapes with a zero of intensity are analytically treatable and advantageous to produce, as the diffraction limit enforces robust parabolic profiles. MINFLUX localizations in one-, two- and three-dimensions have been achieved through beams shaped by half-moon[10], vortex[4] and top-hat[8] phase masks. As even Gaussian beams[4] are efficient when used appropriately, we expect future studies proposing other novel usable beam shapes.

Available lateral scanning technologies include galvanometric scanners, piezoelectric, electro-, and acousto-optic deflectors, while axial scanning technologies include electro-, acousto-optic, and liquid lenses, as well as piezoelectric actuators in remote-focusing configurations. MINFLUX implementations have been based on electro-optical lateral deflection[4], as it is compact, achromatic and simple to use, and delivers sub-nanometer and sub-microsecond deflection, mostly limited by the high-voltage driver bandwidth. For axial deflection, previous implementations have used either an electro-optically tunable lens[8], based on the Kerr effect, or deformable mirrors[12]. The tunable lens is a high capacitance device with a limited focal length of down to one meter and a response in the order of 30 µs, limited by the current provided by its high-voltage amplifier. Deformable mirrors, being micro-electro-mechanical devices, face similar speed constraints.

We present an interferometry-based strategy for fast beam shape manipulation, compatible with continuous-wave and pulsed beams. We study several beam deformation scenarios, many of which result in displacements or tilts of point-, line- and plane-like zeros of intensity, making them attractive for super-resolution techniques such as STED and RESOLFT and localization strategies like MINFLUX

and MINSTED, as well as for optical tweezers applications. We developed and characterized a general-purpose four-channel beam-shaping polarization interferometer, specifically designed for enabling 3D imaging and tracking in a two-color excitation MINFLUX system. The implementation of this technology resulted in the first demonstration of concurrent two-emitter MINFLUX tracking in 3D, subsequent to the recent introduction of simultaneous two-emitter MINFLUX tracking in 2D[13]. These advancements pave the way for multi-emitter MINFLUX tracking as a method for studying the kinetics and conformational states of flexible protein complexes with respect to an absolute origin, free from range limitations present in single-molecule FRET[14] and with time resolutions in the sub-millisecond range, surpassing high-speed AFM[15].

Results

Interferometric manipulation of an intensity zero point, line and plane

Regions of space where focused beams have no intensity exist as points, lines or planes and can be generated by distinct phase masks at the back focal plane of a lens. Near these locations with no intensity, the spatial dependence of the electric field and its polarization take a variety of forms. It is possible to manipulate the shape and location of these regions by interferometrically combining distinct beams, thus mapping their relative amplitudes and phases to spatial features. Figure 1 displays various simulated beam combinations that displace and tilt zero-intensity regions.

Several of these combinations are based on matching pairs of beams with linear and uniform electric fields, see Table 1. For example, a circularly polarized donut beam, created using a 2π vortex mask, features an axial zero line and a linearly dependent electric field across the XY plane that can be laterally displaced when combined with a circularly polarized Gaussian beam (Fig. 1a). As the donut beam contains all phases of electric field at any given time, there will always be a location where it destructively interferes with the Gaussian beam. That location is dictated by the relative amplitude and phase of the Gaussian beam, mapping them to physical polar coordinates[16]. A similar phenomenon occurs with a linearly polarized beam shaped by a half-moon phase mask, creating an axial zero plane that shifts laterally when paired with a linearly polarized Gaussian beam (Fig. 1b). When combining a charge-2 donut beam with a Gaussian beam (Fig. 1c), the axial zero line at the origin splits into two zero lines, opposite from each other, which are also mapped into polar coordinates by the relative phase and amplitude of the beams.

Furthermore, interferometric combinations that specifically alter the axial distribution within the beams can be engineered. For instance, the central zero point of a bottle beam can be axially shifted by combining it with a Gaussian beam (Fig. 1d), as the bottle beam is purely laterally polarized across the z-axis with a linear dependence on z. Other innovative combinations include tilting the axial zero

line of a circularly polarized donut beam (Fig. 1e) and tilting the zero plane of a linearly polarized half-moon beam (Fig. 1d) when combining them with the bottle beam and its linear analogue, respectively. See Table 2 for a list of the beam combinations presented.

However, beams focused with high numerical aperture contain axial electric fields, leading to a zero degradation if (i) the interferometric combination does not yield a null axial component or, if (ii) it does, but its location does not match the zero of the lateral components (see electric field profiles in Fig. 1a-g with zero mismatches marked by arrows). Additionally, a mismatch of Gouy phases, as in the case for the bottle beam and the Gaussian, degrades axially shifted zeros. Such degradation manifests in scenarios involving large displacements of the zero and depends on the numerical aperture of the system and fill factor of the beams.

Despite these circumstances, the interferometric shifting of zeros can imitate whole beam deflection for techniques, such as MINFLUX, where only the parabolic intensity distribution around a zero matters. It offers an enticing alternative to current technologies for implementing axial deflection as discussed in the following section. In brief, it allows to implement 3D MINFLUX operation without diminishing its performance despite the inevitable zero degradation.

A four-channel common-path beam-shaping polarization interferometer

We present an implementation of our interferometric beam shaping strategy with a system that is compact, modular, scalable, cheap, flexible, and capable of dynamic manipulation. This system is designed to meet specific requirements for beam interference: modulation of the amplitude and/or phase of the interfering beams, independent shaping of each beam, and their subsequent interference. The system comprises three main blocks (Fig. 2a-c): a polarization rotator, a beam shaper, and a beam combiner. These components function in parallel over four possible paths (Fig. 2d) which, in this embodiment, are designed to be interleaved, allowing independent shaping and modulation for two laser wavelengths.

The first block, a polarization rotation module (Fig. 2a), allows us to change the relative amplitude of the beams that will interfere. Starting with a linearly polarized Gaussian beam $E_0\mathbf{x}$, the rotator is simply comprised of an electro-optical modulator (EOM) with its principal axis at 45° and an achromatic quarter-waveplate at 0°. This results in orthogonal linearly polarized states $E_1\mathbf{x} + E_2\mathbf{y}$, depicted in yellow and blue, with $E_1 = E_0 \cos\alpha(V)$ and $E_2 = E_0 \sin\alpha(V)$, and V, the voltage applied to the EOM. This combination offers maximal modulation speed and has no chromatic angular dispersion. Implementing phase modulation, e.g., to realize the zero rotations depicted in Fig. 1a, c, e, only requires an additional EOM with a 0° principal axis.

A double-pass configuration on a spatial-light modulator (SLM) independently shapes the wavefront of each orthogonal linear polarization state (in yellow and blue), depicted in fig. 2b as a split diagram around a metallic mirror. The SLM imprints first a programmable retardation $\varphi_1(x,y)$ on E_1 (yellow beam), while the light in the orthogonal polarization state (blue beam) remains ideally unaffected. The following elements—quarter-waveplate, convergent lens and metallic mirror—produce an inverted image of the SLM onto itself, as the system behaves as a $4f$ imaging system, and a 90° rotation of the polarization. This makes the second pass fall on a distinct region of the SLM (not shown in the simplifier diagram of Fig. 2b), adding an arbitrary retardation $\varphi_2(x,y)$ to E_2 (yellow beam) and resulting in an output $E_2 \mathrm{e}^{i\varphi_2(x,y)}\mathbf{x} + E_1 \mathrm{e}^{i\varphi_1(x,y)}\mathbf{y}$.

Finally, both patterned fields E_1 and E_2 undergo a 45° polarization rotation by a half-waveplate and a polarization beam splitter (PBS) produces the final interference (Fig. 2c), outputting $\frac{1}{2}E_1 \mathrm{e}^{i\varphi_1(x,y)} + \frac{1}{2}E_2 \mathrm{e}^{i\varphi_2(x,y)}$. Both interfering beams share their optical path, meaning that this system has no need of active feedback loops or adjustments to maintain the relative phase stability.

It is common practice to use a blazed diffraction grating (e.g., horizontal) on SLM holograms to reject undesirable spurious phase structures imprinted on its zero-th order, i.e., the direct reflection. A common spatial filter for the four paths (shown in Fig. 2d) rejects the zero-th order while the first diffraction order, which carries the patterned beams, passes through. As an added benefit, the use of the first diffraction order in our double-pass configuration filters out the crosstalk between polarization states due to, for example, the imperfect retardation of the quarter-waveplate. Additionally, we apply an orthogonal grating outside of the selected pupil region (fig. 2e) for suppressing spurious light.

The modular geometry described above is replicated to produce four independent paths, each carrying an interferometric mixture of two shaped beams on a single SLM (Fig. 2d). At any given point in time, only one path is meant to be in use. We tailored this system to operate with two paths in the green range (560 nm) and two in the red range (640 nm). After combining both laser sources with a dichroic mirror, an EOM-based path switching selects paths A/B or C/D for red/green. Each path contains its own EOM-based polarization rotator (as in Fig. 2a) followed by a spatial filter for cleaning up the mode. Paths A/B and C/D are split by dichroic mirrors and reach distinct regions of the SLM labeled as A1/B1/C1/D1 (Fig. 2e). The double-pass configuration changes their height and inverts the order of the regions on the second pass to D2/C2/B2/A2. Ultimately, the system can realize any of the beam manipulations previously mentioned in any of the four paths. After interference at the subsequent PBS, all paths are recombined into one and propagate into a MINFLUX confocal microscope, comprised of the commonly required blocks of scanning, detection, and stabilization. The output of the

interferometer is linearly polarized; further manipulations of the polarization state required for MINFLUX operation are common to all paths are produced by further blocks.

In conclusion, for each excitation wavelength it is possible to select one of four phase masks e.g., φ_{A1}, φ_{C1}, φ_{A2}, φ_{C2} and, additionally, it is possible to interferometrically combine two pairs of them e.g., $E_0\left[\chi_A \mathrm{e}^{i\varphi_{A1}} + (1-\chi_A)\mathrm{e}^{i\varphi_{A2}}\right]$ and $E_0[\chi_C \mathrm{e}^{i\varphi_{C1}} + (1-\chi_C)\mathrm{e}^{i\varphi_{C2}}]$, where the mixture coefficients χ_A and χ_C are dictated by the polarization rotation. We exploit this flexibility in the next section.

A fast axial scanner for efficient 3D MINFLUX

MINFLUX localization requires sequentially probing the emission of a fluorophore with tailored excitation beam shapes at distinct locations. Figure 1a shows that an interferometric approach can produce lateral deflections suitable for MINFLUX, however, a pair of electro-optical deflectors surpasses its range at a similar cost with a simpler implementation. Hence, we focus our attention on the axial deflection depicted in Fig. 1d, which has unrivaled time response, and the capability of switching beam shapes and wavelengths. This system can produce a variety of MINFLUX configurations, some of which are shown in Fig. 3a: all Gaussian or donut beams for 2D localization, all deformable bottle beam for 3D localization and mixtures of donut and bottle beams for improved performance, as well as interleaved wavelengths for simultaneous MINFLUX localization in distinct spectral bands (Fig. 3b).

Interferometric axial deflection of the *zero point* of a bottle beam overlapped with a Gaussian beam is shown via single-molecule fluorescence PSF measurements alongside simulations (Fig. 3c). This zero level can degrade due to a lack of coherence, misalignment between the interfering beams and optical aberrations that produce spurious electric field components. Even under ideal conditions, a mismatch in the axial dependence of the Gouy phase of both beams leads to dephasing and prevents perfect destructive interference, hence degrading the zero quality. These effects are dependent on the numerical aperture and fill.

MINFLUX schemes that displace beams with a zero of intensity harvest a gradient of *photon collection probability* that leads to a high localization precision[17]. This is hampered by zero degradation and is equivalent to a loss of signal-to-background ratio. Fig. 3d features a comparison of localization Cramér-Rao Bound (CRB) between defocused bottle beams with perfect zeros and interferometrically deformed bottle beams with zeros that degrades depending on their position. Despite the imperfect zeros there is no major deviation from the ideal localization precision.

Displaced bottle beams provide axial information, yet in the lateral direction they provide poorer performance than donut beams. This is because, as an emitter displaces laterally, the emitted

background *per emitted fluorescence photon* is higher for bottle beams than for donut beams, due to their weaker curvatures, larger size, and axial lobes. One could consider working in low background scenarios, but MINFLUX operates by purposely lowering the signal in exchange for high information content per photon. Thus, one should always strive to work in a regime in which background and/or zero quality are not negligible. We therefore implemented the capability of using a mixture of donut and bottle beams within one MINFLUX excitation pattern for lateral localization and axial localization, respectively. A CRB comparison of both scenarios (Fig. 3e) reveals an up to 2-fold improvement, for a molecule localized at the center of the excitation pattern, as the diameter L shrinks.

The speed of the interferometric deflection is directly dependent on the bandwidth of the polarization rotation depicted in Fig. 2a. In this implementation, we chose an electro-optical modulator, whose rise time is limited by the bandwidth and electrical current of the driving amplifier. We determined the rise time of the axial deflection by using gold nanoparticles to image the transient PSF via elastic scattering detection at a time resolution of 200 ns (Fig. 3f). We measured a rise time (10%-90%) of <1.1 µs and a stabilization time (<1% of the asymptote) of <2.5 µs, with a system delay of 1.6 µs.

MINFLUX imaging and tracking

For proof-of-principle demonstrations of the system we used static and dynamic DNA origami structures as well as fixed cell samples. First, we designed and folded a DNA origami that arranges 12 Alexa Fluor 647 dye molecules in a three by four grid with 20 nm spacings for 3D imaging (see MINFLUX imaging of DNA origami). The results are shown in Fig. 4a: all sites are clearly resolved with a Full Width at Half Maximum (FWHM) of the fitted Gaussian distribution of <3 nm in xy and <5 nm in z corresponding to standard deviations for the localization precision of <1.3 nm and <2.1 nm, respectively. Furthermore, we acquired 3D images of the nuclear pore complex (NPC) by labelling SNAP-tagged NUP96 with Alexa Fluor 647 in fixed U-2 OS cells, see Fig. 4b.

To showcase the 3D tracking capability and temporal resolution of the system, we designed a DNA origami with a fluorescently labelled axially oscillating DNA strand. The DNA origami is rod-like, approximately 50 nm-tall, and features 16 biotin-modified DNA staple strands for it to stand vertically on streptavidin-functionalized surfaces (Fig. 4c). Localization traces shown in Fig. 4c are at 1 ms and 10 ms temporal binning, which correspond to 150 and 1500 average photon counts per localization, respectively. At 1 ms temporal resolution, the standard deviations for the localization precisions are 4.9, 4.7 and 4.1 nm in x, y and z, and the distance in z between binding sites, 12.8 ± 5.6 nm.

The measurement scheme for tracking consisted of a first step where the excitation pattern is centered onto the fluorophore via an active feedback loop that uses the live estimated localization. This feedback loop can flexibly act on either the tip-tilt mirror, the EODs, or both scanners simultaneously.

We chose the former because it is de-scanned and hence the collection efficiency is optimal after centering in a range of less than 10 nm from the fluorophore location. Once centered, the excitation pattern is static over time and probes the molecule until photobleaching. The performance of the centering can be appreciated in the localization traces, with the center of the excitation sequence after convergence setting the origin in all dimensions.

Finally, we utilized the two-color excitation of our MINFLUX implementation to simultaneously track two spectrally distinct emitters (ATTO 647N and Janelia Fluor 549 dyes) on a DNA origami structure with programmable dynamics for both of them (Fig. 4d). The average photon counts per localization in the displayed localization traces is 1200 for both emitters, resulting in 20 ms temporal resolution for ATTO 647N and 25 ms for Janelia Fluor 549. The corresponding standard deviations for the xyz-localization precisions are 2.2, 2.3, 1.8 nm for ATTO 647N and 1.8, 1.7, 1.6 nm for Janelia Fluor 549.

In this case, the measurement scheme involved a centering step at 640 nm excitation wavelength, converging onto the far-red dye, and defining a volume that encompasses both emitters. Following centering, the two excitation lasers were interleaved in time to probe the emitters with static excitation patterns, each one lasting approx. 250 µs. Notably, the fast deflections by the EODs and the axial interferometer would allow decreasing this excitation sequence length if the application required it.

Discussion

We presented an interferometric strategy to manipulate a variety of focused beams, including some that are newly described. Our efforts centered on beams with intensity zeros and the manipulation of these regions through displacements and tilts. We proposed general optical blocks that translate polarization rotations into beam deformations via polarization interferometry of holographically-shaped beams. A specific optical design of a four-channel interferometric beam-shaping system was introduced and employed as the excitation of a MINFLUX localization microscope. We utilized the system for super-resolution imaging as well as single- and multi-molecule tracking, reaching state-of-the-art localization precision and time resolution, and introduced novel MINFLUX schemes and dual-color operation.

The proposed system is based on a highly versatile and easily extendable common-path polarization interferometer, notable for its phase stability without active feedback. Its implementation is devoid of mechanical parts and manipulates beams at the microsecond time scale. However, slower and more economic polarization rotation technologies are also compatible, such as mechanical- or liquid-crystal-based methods.

Alternative approaches, such as using a polarization rotator and a custom birefringent patterned mask (commercially available), could achieve similar interferometric effects. This mask would imprint tailored phase structures, partially replacing the SLM role. However, it is limited to a fixed wavelength and lacks the ability to correct aberrations or adjust phases. A single-pass configuration using an SLM could ideally allow all interferometric pairs involving a Gaussian beam by using the modulator's unaffected polarization. Nevertheless, this approach excludes blazed gratings, which would eliminate native phase structures from the SLM. Additionally, the lack of fine alignment and aberration corrections on the Gaussian direct reflection leads to zero degradation, non-linear axial calibration and unintended tilts.

MINSTED, a recent approach for single-molecule localization analogous to MINFLUX, leverages the enhanced position information encoded in the effective point spread function of a STED microscope. Applying our axial displacement strategy to a STED beam is optimally suited for extending MINSTED into the axial dimension, as well as for applications of conventional fast STED imaging, especially for imaging small volumes.

We anticipate the development of pulsed interleaved MINFLUX implementations with deformed and axially deflected bottle beams. This could potentially be combined with lateral electro-optical (or other) deflections, although utilizing many pulses is complex and limits power. We envision similar configurations to incorporate more wavelengths or beam shapes, and to combine them with high-speed SLMs for adaptive beam changes on the millisecond scale.

A major strength of MINFLUX localization is its isotropic performance in three dimensions, unlocking new possibilities for single-molecule assays, and its iterative version, which maximizes spatial information extraction. However, custom implementations have primarily focused on two-dimensional static MINFLUX, presumably due to its complexity. We believe that implementations following the approach presented here, along with expected further improvements and simplifications, might pave the way for broader adoption of this technology at its full capability beyond current commercial solutions.

Acknowledgements

We thank Karina Arellano Ayala for assistance with sample preparation. We thank Anna Deputatova for assistance with designing and folding the 32HB origami.

This project has received funding from the European Research Council (ERC) under the European Union’s Horizon 2020 research and innovation program (Grant agreement No. 853348).

For the purpose of Open Access, the authors have applied a CC BY public copyright license to any Author Accepted Manuscript (AAM) version arising from this submission.

Author Contributions

M.K.G., A.G. and F.B. designed and built the system, and programmed the hardware control. M.K.G., A.G., A.P., M.S. and F.B. programmed the processing and visualization software. M.K.G. and A.G. performed experiments and data analysis. A.P. designed and folded DNA origami and optimized used protocols. A.P. prepared and optimized cell samples. M.S. performed simulations and optimizations. M.K.G., A.G., A.P. and F.B. wrote the manuscript. F.B. supervised the project.

Competing Interests

F.B. holds patents on principles, embodiments and procedures of MINFLUX.

Figure 1

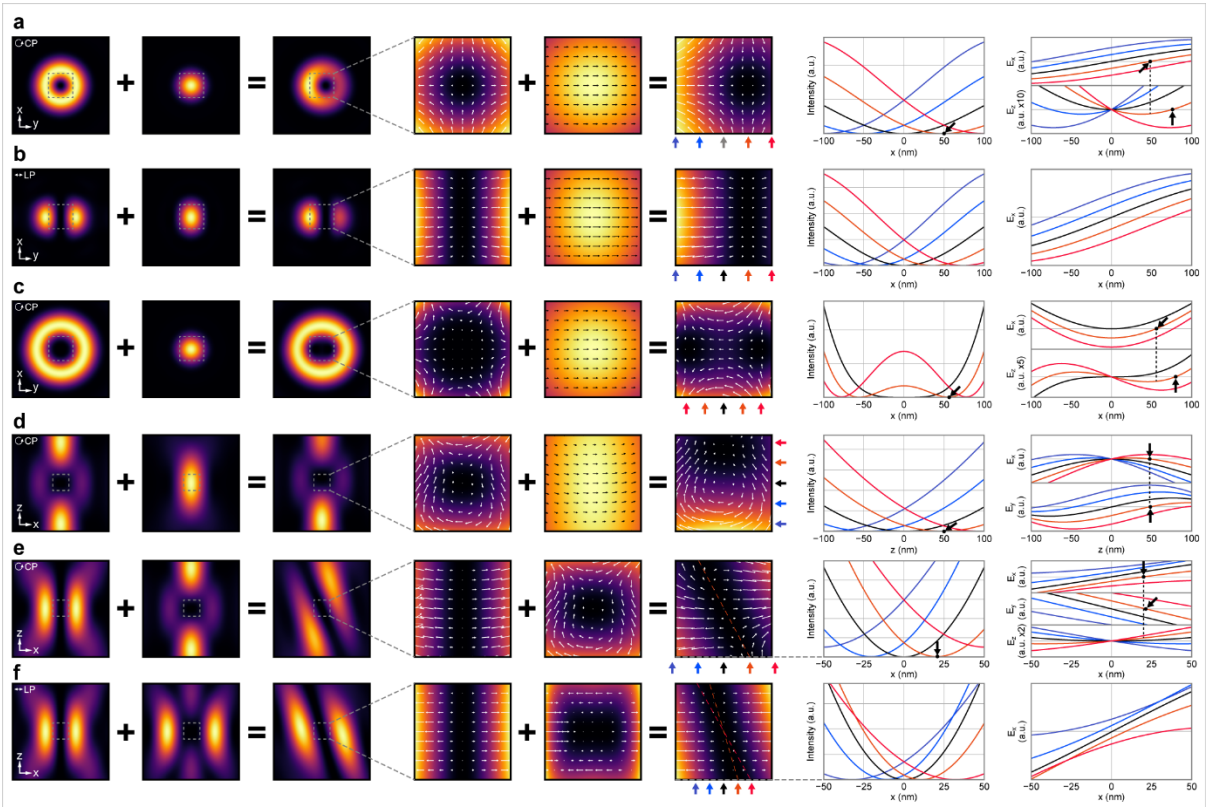

Fig. 1: Interference of canonical beams. a, Combination of charge-1 donut with Gaussian beams. **b**, Combination of half-moon and Gaussian beams. **c**, Combination of charge-2 donut and Gaussian beams. **d**, Combination of bottle and Gaussian beams. **e**, Combination of charge-1 donut and bottle beams. **f**, Combination of half-moon and linearly polarized analog of bottle beam. (Left column) Intensities of combined beams at the XY (a-c, 400x400nm) and XZ (d-f, 600x600nm) plane. CP: circularly polarized. LP: linearly polarized. Dashed squares: 100x100nm. (Middle column) Zoomed intensities in the dashed squares with a vector plot of the XY (a-c) or XZ (d-f) components of the electric field. The resulting displaced zero coordinate is marked by an arrow. (Right column) Intensity and electric field profiles for each X, Y and/or Z component along the x axis (a-c), z axis (d) or x axes offset in z (e,f), chosen to highlight the interplay between electric field components. Mismatches between zeros of different components are marked with arrows.

Figure 2

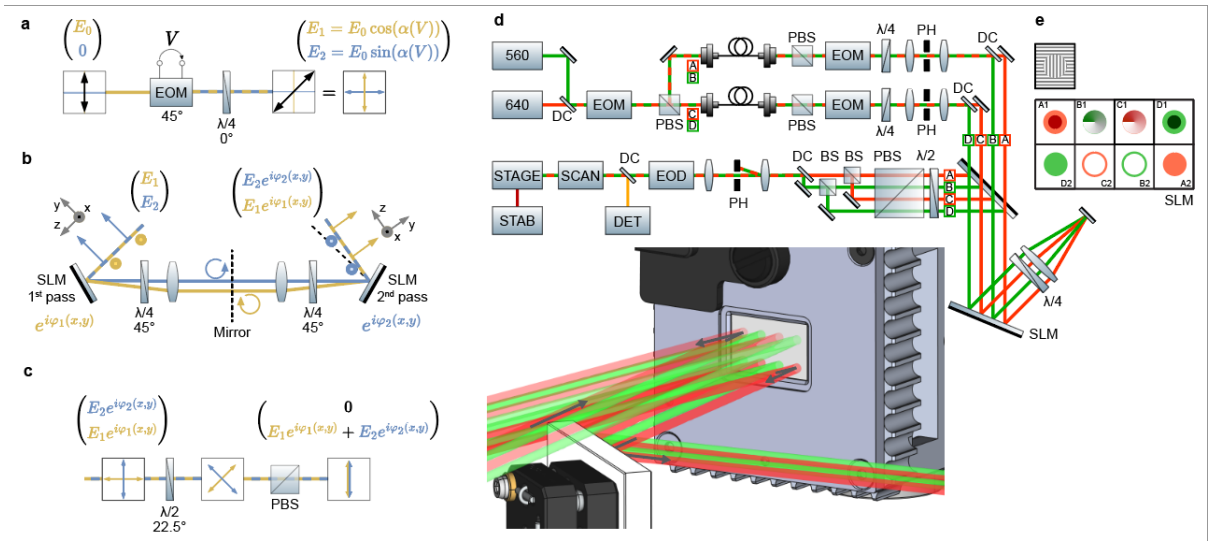

Fig. 2: Implementation of a multi-channel polarization interferometer. **a**, Polarization rotation module. The square with arrows represents the polarization state. **b**, Simplified diagram of the beam shaping module. A double-pass configuration on an SLM is shown unfolded with respect to its mirror. **c**, Beam combination/interference module. **d**, Complete system. **e**, Detailed grating structure used in all SLM regions (above), example phase masks (below) for interferometric bottle beam deflection in A1+A2 (and D1+D2) and donut beam generation on B1 (and C1) for red (and green) wavelengths; B2 and C2 are unused.

Figure 3

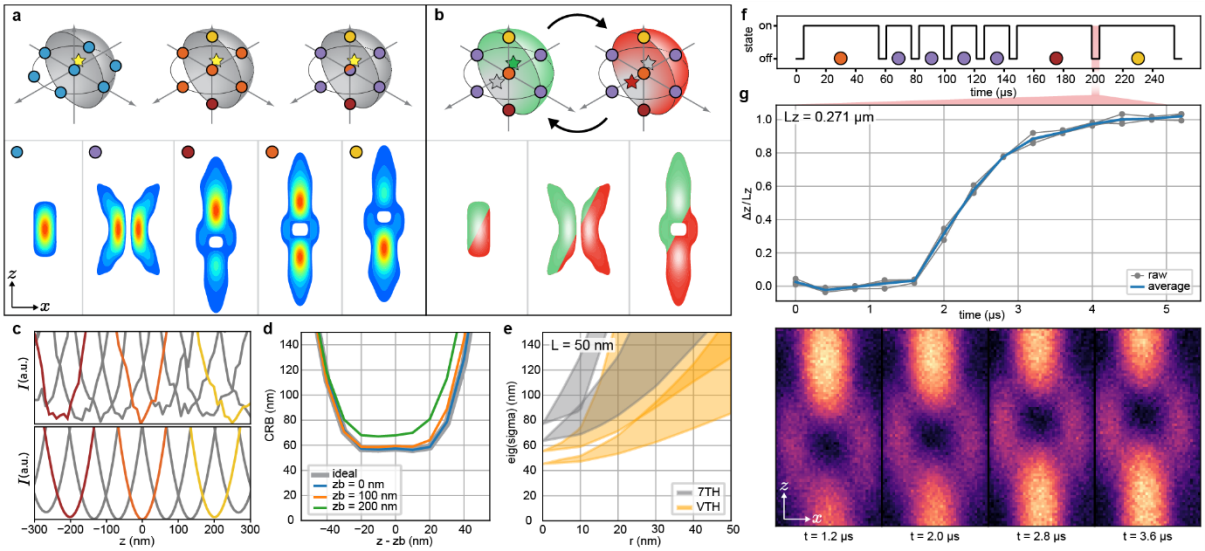

Fig. 3: MINFLUX schemes with interferometrically deformed beams and mixed shapes. **a**, Depiction of the 2D and 3D MINFLUX schemes realized with our system (top) and their corresponding beam shapes (bottom): Gaussian beam (blue), donut beam (purple) and bottle beam (red, orange, yellow) at different interferometric deflection states. **b**, Scheme for tracking two emitters simultaneously by rapidly switching between patterns for red and green excitations wavelengths, with seven exposures each. **c**, Juxtaposition of simulated (top) and measured (bottom) intensity profiles of the deflected bottle beam zero. Despite the deformation, the profiles stay parabolic over a large range. The unavoidable zero degradation is visible towards the edges. **d**, Comparison of the CRB along the optical axis z for ideally deflected bottle beams (without deformation, gray) and for our interferometric approach. Only when localizing emitters far off focus, given by the axial distance zb, the performance degrades slightly. **e**, CRBs of the *mixed beam* scheme with donut and bottle beams (VTH) versus the conventional 3D MINFLUX scheme consisting only of bottle beams (7TH). Each condition displays two shaded areas, one for the minimum and one for the maximum CRB eigenvalue, indicating anisotropy; the width each area accounts for spatial inhomogeneity. **f**, Timing diagram for the mixed beam scheme, with larger weights for the bottle beam exposures. **g**, Measurement of the interferometric deflection transient (top). Each point corresponds to the location of the zero of intensity obtained from a complete PSF measurement (bottom, selected time points).

Figure 4

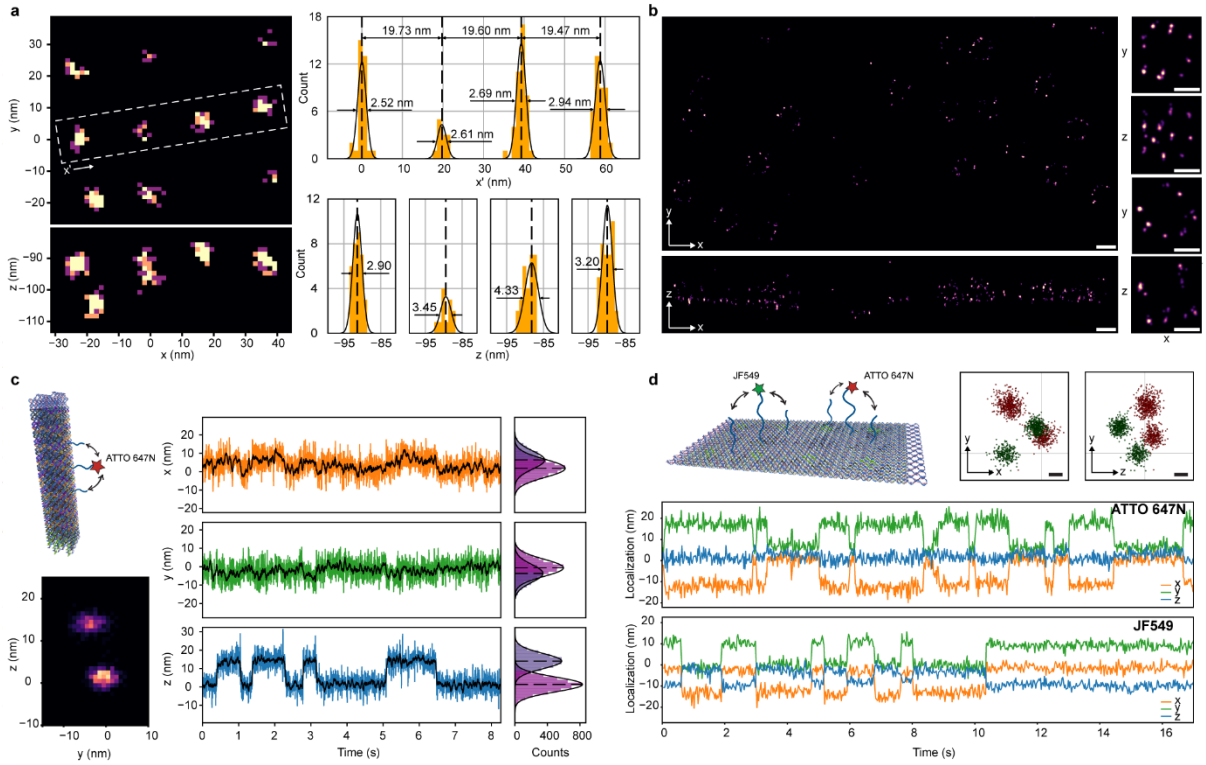

Fig. 4: MINFLUX imaging and tracking. **a**, 3D Imaging of Alexa Fluor 647 fluorophores arranged in a 3x4 grid with 20 nm spacing on a DNA origami (left). Localization histogram along the marked region with indications for distances and FWHM (top right) and corresponding histograms along z for each site (bottom right). **b,** 3D imaging of NUP96-SNAP labelled with BG-Alexa Fluor 647 in fixed U-2 OS cells. **c**, 3D tracking of ATTO647N conjugated to a DNA strand that oscillates axially between two binding sites on a DNA origami (top left). Histogram of localizations at 10 ms temporal resolution (bottom left). Localization traces for each coordinate (middle) at 1 ms temporal resolution (x: orange, y: green, z: blue) and with 10-fold temporal binning (black). Histograms for the two distinct positions of the molecule (right). **d**, Schematic of a 2D origami (upper left) with ATTO647N and Janelia Fluor 549 dyes, each transiently binding to two distinct sites. XY and YZ projections (upper right) of all localizations in the traces displayed below. Localization traces for ATTO647N and Janelia Fluor 549 (bottom), at 20 ms and 25 ms temporal resolution, respectively. DNA origami renders were generated with oxView. Scale bars: (**b**) 100 nm for large field of view, 50 nm for single pores, (**d**) 5 nm.

Table 1

Beam	Polarization	Phase mask	Zero type	$\boldsymbol{E_x(\vec{r})}$	$\boldsymbol{E_y(\vec{r})}$	$\boldsymbol{E_z(\vec{r})}$
Gaussian	Circular	Flat	None	1	i	$x - iy$
Gaussian	Linear	Flat	None	1	0	x
Half-moon	Linear	Half-moon	Transverse plane	x	0	$-ixy$
Donut charge 1	Circular	Vortex 2π	Axial line	$x + iy$	$ix - y$	$-x^2 + y^2 + 2ixy$
Donut charge -1	Circular	Vortex -2π	None	$x - iy$	$ix + y$	1
Donut charge 2	Circular	Vortex 4π	Axial line	$-x^2 + y^2 + 2ixy$	$i(-x^2 + y^2) - 2xy$	
Bottle	Circular	Top hat	Point	$x^2 + y^2 + z$	$i[x^2 + y^2 + z]$	$ix - y$

Table 1. Canonical beam shapes with their polarization state, corresponding back-focal plane phase mask and zero type. Minimal order approximations of the focused electric field at the origin are shown for each component of the electric field.

Table 2

Beam 1	Beam 2	Polarization state	Zero type	Result
Donut charge 1	Gaussian	Circular	Axial line	Lateral displacement
Half-moon	Gaussian	Linear	Axial plane	Lateral displacement
Donut charge 2	Gaussian	Circular	Axial line	Lateral displacement Double lines
Bottle	Gaussian	Circular	Point	Axial displacement
Donut charge 1	Bottle	Circular	Axial line	Line tilt
Half-moon	Bottle (linear)	Linear	Axial plane	Plane tilt

Table 2. Beam combinations presented in this work.

356 # References

357

358 1. Hell, S. W. & Wichmann, J. Breaking the diffraction resolution limit by stimulated emission:
359 stimulated-emission-depletion fluorescence microscopy. *Opt. Lett.* **19**, 780 (1994).
360 2. Hell, S. W., Jakobs, S. & Kastrup, L. Imaging and writing at the nanoscale with focused visible light
361 through saturable optical transitions. *Appl. Phys. Mater. Sci. Process.* **77**, 859–860 (2003).
362 3. Masullo, L. A. *et al.* Enhanced photon collection enables four dimensional fluorescence nanoscopy
363 of living systems. *Nat. Commun.* **9**, 3281 (2018).
364 4. Balzarotti, F. *et al.* Nanometer resolution imaging and tracking of fluorescent molecules with
365 minimal photon fluxes. *Science* **355**, 606–612 (2017).
366 5. Weber, M. *et al.* MINSTED fluorescence localization and nanoscopy. *Nat. Photonics* **15**, 361–366
367 (2021).
368 6. Rust, M. J., Bates, M. & Zhuang, X. Sub-diffraction-limit imaging by stochastic optical
369 reconstruction microscopy (STORM). *Nat. Methods* **3**, (2006).
370 7. Betzig, E. *et al.* Imaging intracellular fluorescent proteins at nanometer resolution. *Science* **313**,
371 (2006).
372 8. Gwosch, K. C. *et al.* MINFLUX nanoscopy delivers 3D multicolor nanometer resolution in cells. *Nat.*
373 *Methods* **17**, 217–224 (2020).
374 9. Eilers, Y., Ta, H., Gwosch, K. C., Balzarotti, F. & Hell, S. W. MINFLUX monitors rapid molecular jumps
375 with superior spatiotemporal resolution. *Proc. Natl. Acad. Sci. U. S. A.* 201801672 (2018)
376 doi:10.1073/pnas.1801672115.
377 10. Wolff, J. O. *et al.* MINFLUX dissects the unimpeded walking of kinesin-1. *Science* **379**, 1004–1010
378 (2023).
379 11. Deguchi, T. *et al.* Direct observation of motor protein stepping in living cells using MINFLUX.
380 *Science* **379**, 1010–1015 (2023).

12. Schmidt, R. *et al.* MINFLUX nanometer-scale 3D imaging and microsecond-range tracking on a common fluorescence microscope. *Nat. Commun.* **12**, 1478 (2021).
13. Fiona Cole *et al.* Super-Resolved FRET and Co-Tracking in pMINFLUX. *bioRxiv* 2023.03.24.534096 (2023) doi:10.1101/2023.03.24.534096.
14. Bauer, B. W. *et al.* Cohesin mediates DNA loop extrusion by a “swing and clamp” mechanism. *Cell* **184**, 5448-5464.e22 (2021).
15. Katan, A. J. & Dekker, C. High-Speed AFM Reveals the Dynamics of Single Biomolecules at the Nanometer Scale. *Cell* **147**, 979–982 (2011).
16. Satyajit Maji, Jacob, P. & Brundavanam, M. M. Geometric Phase and Intensity-Controlled Extrinsic Orbital Angular Momentum of Off-Axis Vortex Beams. *Phys. Rev. Appl.* **12**, 054053 (2019).
17. Balzarotti, F. *et al.* Nanometer resolution imaging and tracking of fluorescent molecules with minimal photon fluxes. *Science* **355**, 606–612 (2017).

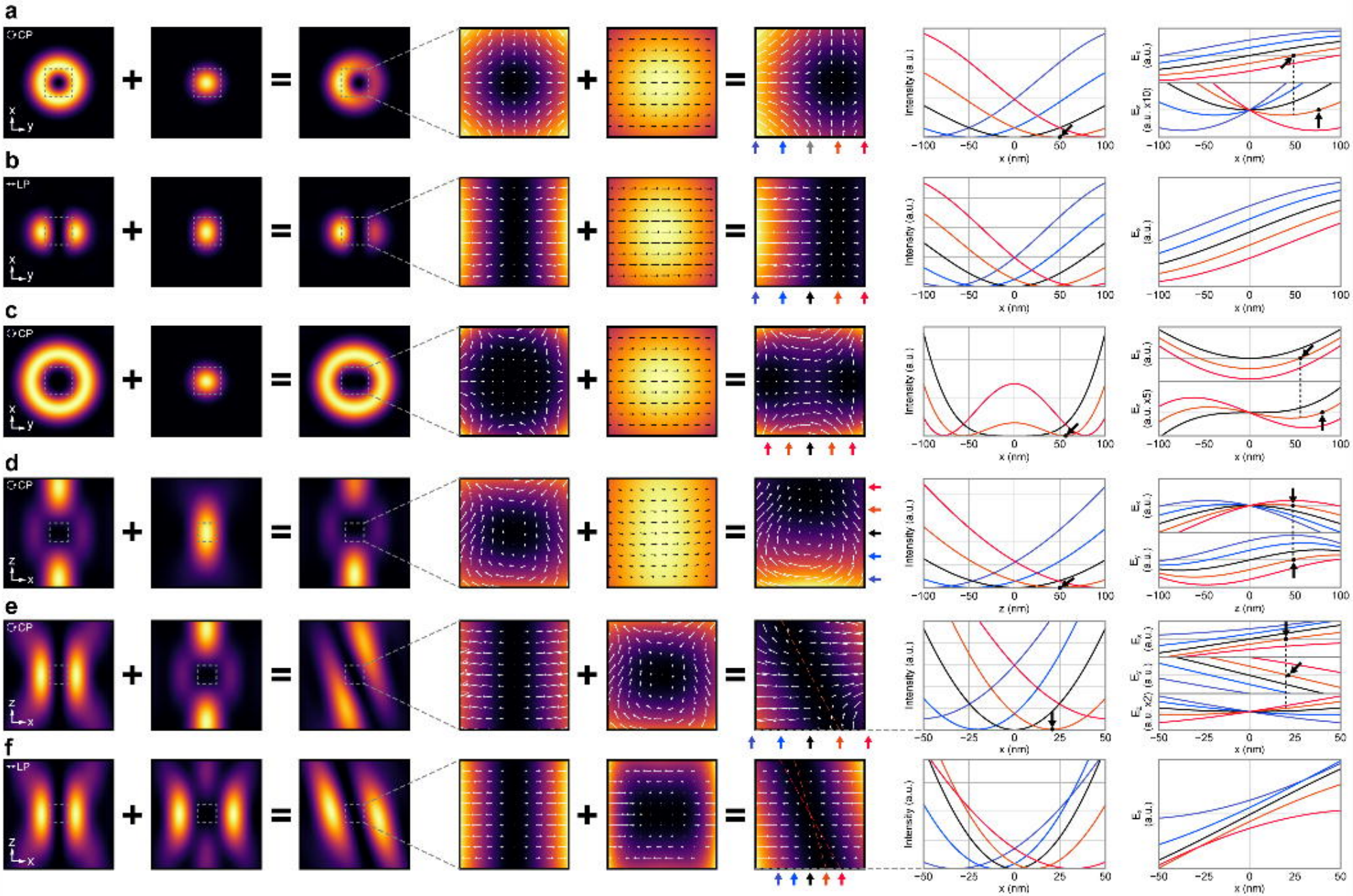
a
b
c
d
e
f
CP
LP
Intensity (a.u.)
x (nm)
z (nm)

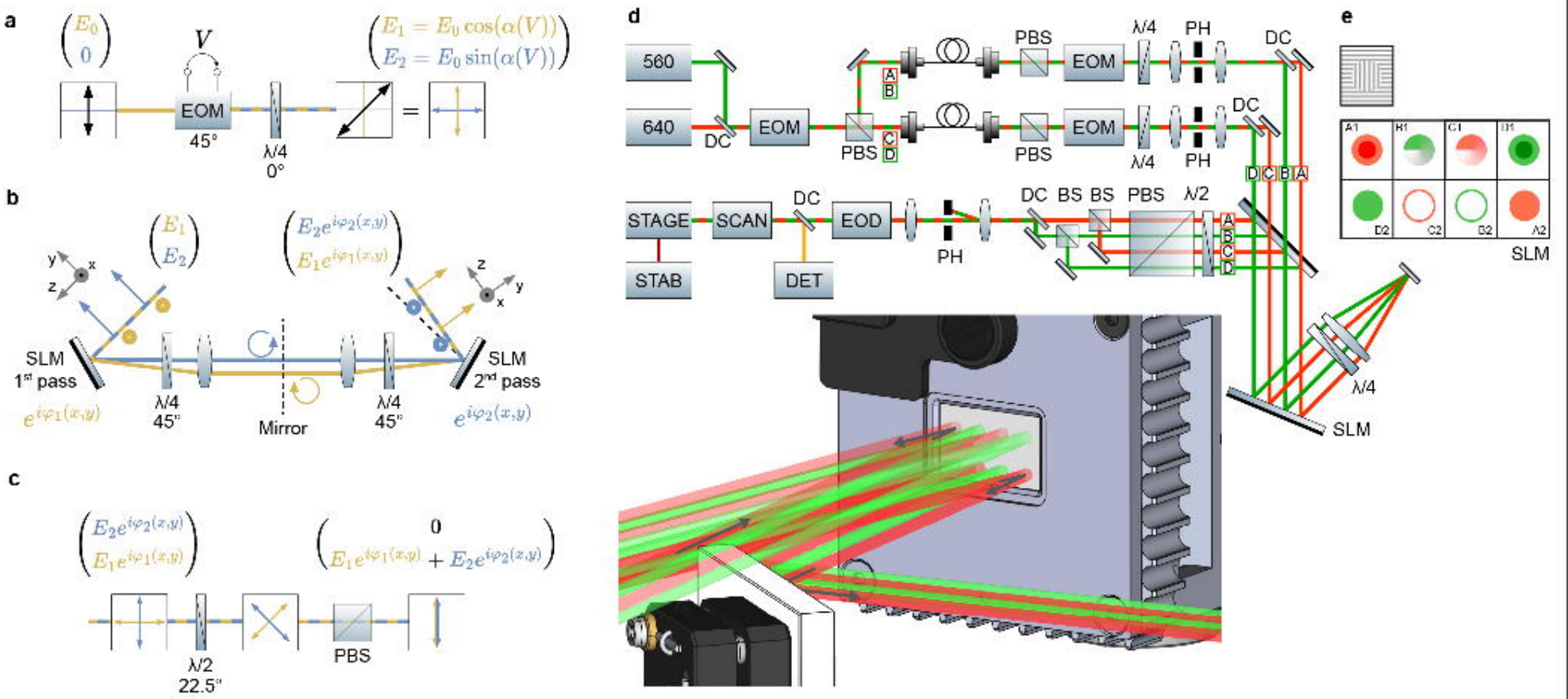
a
$\begin{pmatrix} E_0 \\ 0 \end{pmatrix}$
V
EOM
45°
λ/4
0°
$\begin{pmatrix} E_1 = E_0\cos(\alpha(V)) \\ E_2 = E_0\sin(\alpha(V)) \end{pmatrix}$
=
b
$\begin{pmatrix} E_1 \\ E_2 \end{pmatrix}$
$\begin{pmatrix} E_2 e^{i\varphi_2(x,y)} \\ E_1 e^{i\varphi_1(x,y)} \end{pmatrix}$
SLM
1st pass
$e^{i\varphi_1(x,y)}$
λ/4
45°
Mirror
λ/4
45°
SLM
2nd pass
$e^{i\varphi_2(x,y)}$
c
$\begin{pmatrix} E_2 e^{i\varphi_2(x,y)} \\ E_1 e^{i\varphi_1(x,y)} \end{pmatrix}$
$\begin{pmatrix} 0 \\ E_1 e^{i\varphi_1(x,y)} + E_2 e^{i\varphi_2(x,y)} \end{pmatrix}$
λ/2
22.5°
PBS
d
560
640
DC
EOM
PBS
A
B
C
D
PBS
EOM
λ/4
PH
DC
PBS
EOM
λ/4
PH
DC
D C B A
STAGE
STAB
SCAN
DET
DC
EOD
PH
DC BS BS PBS λ/2
A
B
C
D
λ/4
SLM
e
A1
B1
C1
D1
D2
C2
B2
A2
SLM

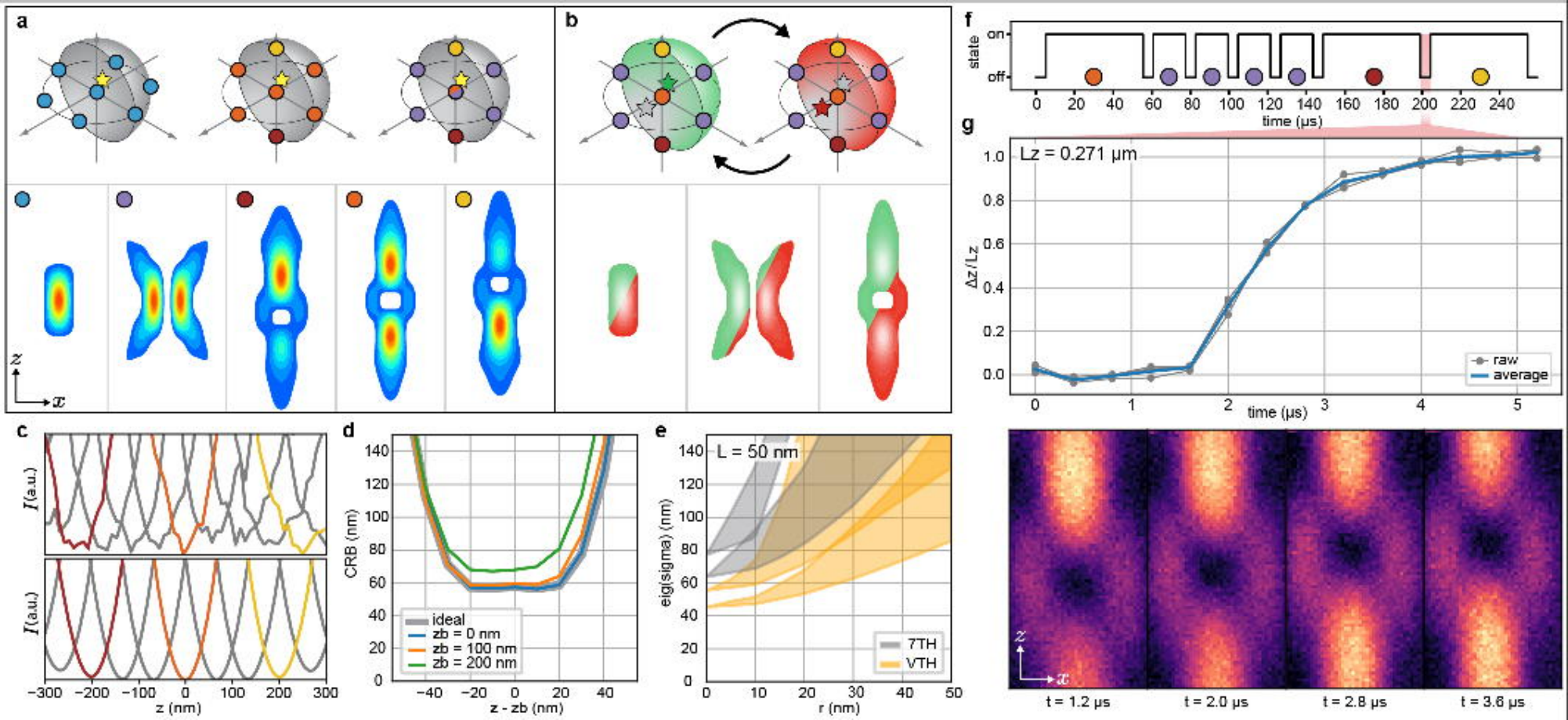
a
b
z
x
f
state
on
off
0 20 40 60 80 100 120 140 160 180 200 220 240
time (μs)
g
Lz = 0.271 μm
Δz / Lz
1.0 0.8 0.6 0.4 0.2 0.0
0 1 2 3 4 5
time (μs)
raw
average
c
I (a.u.)
I (a.u.)
−300 −200 −100 0 100 200 300
z (nm)
d
CRB (nm)
140 120 100 80 60 40 20 0
ideal
zb = 0 nm
zb = 100 nm
zb = 200 nm
−40 −20 0 20 40
z - zb (nm)
e
L = 50 nm
eig(sigma) (nm)
140 120 100 80 60 40 20 0
7TH
VTH
0 10 20 30 40 50
r (nm)
z
x
t = 1.2 μs
t = 2.0 μs
t = 2.8 μs
t = 3.6 μs

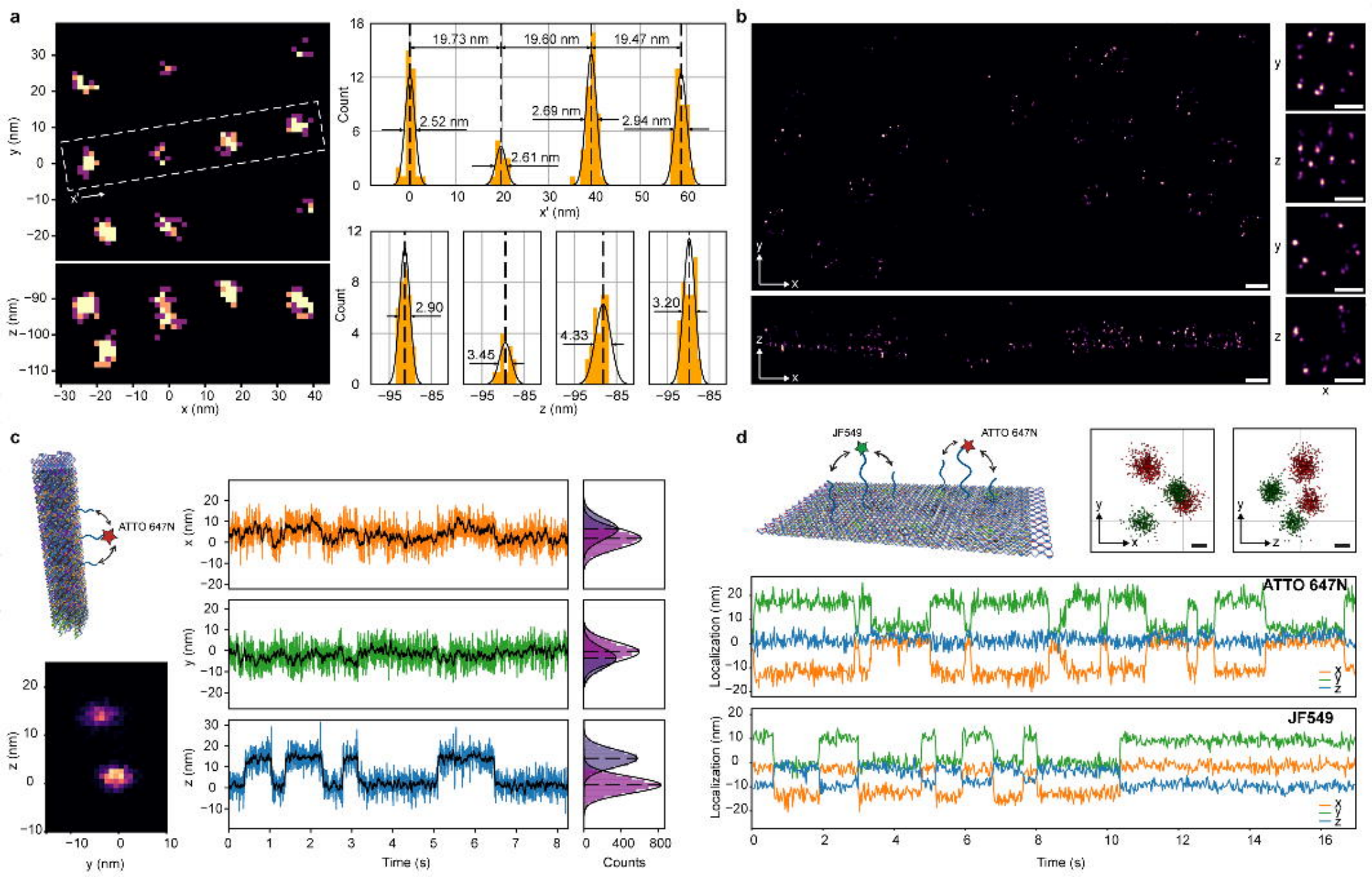
a
y (nm)
x (nm)
z (nm)
x'
Count
x' (nm)
19.73 nm
19.60 nm
19.47 nm
2.52 nm
2.61 nm
2.69 nm
2.94 nm
2.90
3.45
4.33
3.20
z (nm)
b
y
x
z
c
ATTO 647N
y (nm)
z (nm)
x (nm)
Time (s)
Counts
d
JF549
ATTO 647N
Localization (nm)
Time (s)